THE JOURNAL OF BIOLOGICAL CHEMISTRY
Vol. 277, No. 37, Issue of September 13, pp. 34443–34450, 2002

Printed in U.S.A.

Solution Structure of Peptide Toxins That Block Mechanosensitive Ion Channels*

Received for publication, March 20, 2002, and in revised form, May 23, 2002
Published, JBC Papers in Press, June 24, 2002, DOI 10.1074/jbc.M202715200

Robert E. Oswald‡§, Thomas M. Suchyna¶, Robert McFeeters‡, Philip Gottlieb¶, and Frederick Sachs¶

From the ‡Department of Molecular Medicine Cornell University Ithaca, New York 14853 and the ¶Department of Physiology and Biophysics, State University of New York at Buffalo, Buffalo, New York 14214

Mechanosensitive channels (MSCs) play key roles in sensory processing and have been implicated as primary transducers for a variety of cellular responses ranging from osmosensing to gene expression. This paper presents the first structures of any kind known to interact specifically with MSCs. GsMTx-4 and GsMtx-2 are inhibitor cysteine knot peptides isolated from venom of the tarantula, *Grammostola spatulata* (Suchyna, T. M., Johnson, J. H., Hamer, K., Leykam, J. F., Gage, D. A., Clemo, H. F., Baumgarten, C. M., and Sachs, F. (2000) *J. Gen. Physiol.* 115, 583–598). Inhibition of cationic MSCs by the higher affinity GsMtx-4 (K_D ~500 nM) reduced cell size in swollen and hypertrophic heart cells, swelling-activated currents in astrocytes, and stretch-induced arrhythmias in the heart. Despite the relatively low affinity, no cross-reactivity has been found with other channels. Using two-dimensional NMR spectroscopy, we determined the solution structure of GsMTx-4 and a lower affinity (GsMTx-2; K_D ~6 μM) peptide from the same venom. The dominant feature of the two structures is a hydrophobic patch, utilizing most of the aromatic residues and surrounded with charged residues. The spatial arrangement of charged residues that are unique to GsMTx-4 and GsMTx-2 may underlie the selectivity of these peptides.

All cells are responsive to mechanical stimulation, and mechanosensitive ion channels (MSCs)[1] are the most sensitive transducers (1). In higher animals, *exteroceptors* transduce external stimuli such as sound, vibration, touch, and local gravity, whereas *interoceptors* provide feedback for the voluntary musculature and autonomic signals that provide information on filling of the hollow organs (blood pressure regulation, filling of the bladder, etc.). Interoceptors include cellular transducers that permit local control of blood flow, dilation-induced changes in heart rate, and regulation of cell volume and thirst; hormonal-coupled transducers that convert mechanical stimuli into release of factors such as renin and atrial naturietic factor; and autocrine and paracrine transducers that are responsible for local secretion of agents such as endothelin and other growth factors and gene regulators that affect cell division and cell size, as in bone and muscle growth. MSCs are the only known primary mechanical transducers and may drive many of these processes. The three-dimensional structure of a bacterial MSC is known (2), but in eukaryotes, the only MSCs that have been cloned are a family of K^+-selective channels (3–5). The number of different subtypes of MSCs in eukaryotes is unknown. They can be classified in a broad spectrum as stretch-activated channels (SACs) and stretch-inactivated channels. Some of each are K^+-selective, and others are nonselective cation channels (6).

Despite the widespread nature of mechanical transduction in biology, no specific activator or inhibitors of MSCs have been known until recently. Gd^{3+} (10–20 μM) inhibits SACs in both plant and animal cells, suggesting a functional homology between the channels, but Gd^{3+} is not specific for SACs; nor can it be considered a useful lead compound for the development of therapeutic agents. Furthermore, it is not clear if the effects of Gd^{3+} are directly on SACs or mediated by a stiffening of membrane lipids (7–9). Both amiloride (10–13) and some cationic antibiotics (11) can inhibit SACs, but again they lack specificity. Recently, we discovered a family of peptides from the venom of the Chilean rose tarantula, *Grammostola spatulata*, that inhibit SACs in astrocytes and heart cells. The more potent of these toxins, GsMTx-4, not only blocks MSC currents seen with patch clamp recording but exhibits effects at the cellular level that appear to involve MSC activation. GsMTx-4 can reduce the cell size in swollen and hypertrophic heart cells, decrease volume-activated currents in astrocytes (14), and inhibit stretch-induced arrhythmias in the heart (15).

We have determined the solution structure of GsMTx-4 and a lower affinity inhibitor (GsMTx-2) using homonuclear and heteronuclear two-dimensional NMR spectroscopy. The backbone folds of both peptides exhibit the inhibitor cysteine knot (ICK) motif, which is characteristic of a family of invertebrate toxins directed toward a variety of ion channels (16, 17) as well as at least one mammalian protein (18). A dominant feature of the structures is a hydrophobic patch, similar to that described for Hanatoxin (19), encompassing most of the aromatic residues that have been suggested to be important for toxin-recep-

* This work was supported in part by Grant RO1-012042 from the National Institutes of Health and by the ICORP/Japanese Science and Technology Corporation (to F. S.). The costs of publication of this article were defrayed in part by the payment of page charges. This article must therefore be hereby marked "*advertisement*" in accordance with 18 U.S.C. Section 1734 solely to indicate this fact.

The atomic coordinates and structure factors (code 1LQR for GsMTx4; code 1LUP for GsMTx-2) have been deposited in the Protein Data Bank, Research Collaboratory for Structural Bioinformatics, Rutgers University, New Brunswick, NJ (http://www.rcsb.org/).

Sequences for GsMTx-4 and GsMTx-2 have been deposited in the Protein Information Resource (PIR) at the National Biomedical Research Foundation (NBRF), Georgetown (A59403: GsMTx-2; A59371: GsMTx-4).

§ To whom correspondence should be addressed: Dept. of Molecular Medicine, C3 167 Veterinary Medical Center, Cornell University, Ithaca, NY 14853. Tel.: 607-253-3877; Fax: 607-253-3659; E-mail: reo1@cornell.edu.

[1] The abbreviations used are: MSC, mechanosensitive channel; COSY, correlation spectroscopy; GsMTx-2 and GsMTx-4, mechanotoxins from *G. spatulata* venom; HSQC, heteronuclear single quantum correlation; ICK, inhibitor cysteine knot; NOE, nuclear Overhauser effect; NOESY, NOE spectroscopy; SAC, stretch-activated channel; TOCSY, total correlation spectroscopy; HPLC, high pressure liquid chromatography; r.m.s., root mean square; BNPS, 3-bromo-3-methyl-2[(2-nitrophenyl)thiol]-3H-indole.

tor interaction. As with Hanatoxin, MSC peptides have charged residues surrounding the hydrophobic patch, but the distribution of the charges differs between GsMTx-4 and GsMTx-2, suggesting structural correlates that may account for differences in affinity. Hanatoxin is ineffective on MSCs. The ICK motif can be viewed as a well defined scaffold upon which side chains are placed to produce specificity for a particular target. Knowing the structure of MSC-directed ICK peptides, we can design modified structures that are labeled with various indicators, peptides that have higher affinity, and peptides that have differing specificity within the family of MSCs. A high affinity tag may allow isolation of this very difficult group of ion channels.

MATERIALS AND METHODS

Toxin Isolation—The method for venom fractionation and toxin isolation is described in detail by Suchyna *et al.* (14). Briefly, *G. spatulata* (Theraphosidae) spider venom was produced by an electrical milking procedure (20) and stored at −80 °C. The venom was fractionated by high performance liquid chromatography, incorporating Beckman System Gold 126 solvent delivery and 168 photodiode array detector modules (Beckman Instruments, Fullerton, CA) using linear gradients of solvent A (0.1% trifluoroacetic acid in water) and solvent B (0.1% trifluoroacetic acid in acetonitrile). A Zorbax RX-C8 (9.4 × 250 mm, 5 μm, 300 Å; Mac-Mod Analytical, Inc., Chadds Ford, PA) reversed-phase column was used in conjunction with a 40-min linear gradient (15–55% B) with a flow rate of 3.5 ml/min. Fractions were lyophilized and tested for MSC blocking activity on outside-out patches. Fractions that tested positive were further fractionated with slower gradients on a Vydac C18 column (10 × 250 mm, 5 μm, 300 Å; The Separations Group, Hesperia, CA) until a single component was isolated that showed blocking activity. The purity of specific peaks was assessed by analytical chromatography on a Jupiter C18 column (4.6 × 150 mm, 5 μm, 300 Å; Phenomenex, Torrance, CA) with a 40-min gradient of 20–28% B. The average yield of GsMTx-4 and GsMTx-2 from several purifications was ~8 and ~24 mg/ml of venom fractionated, respectively. Thus, GsMTx-4 is at least 2 mM in whole venom, whereas GsMTx-2 is at least 6 mM.

Mass Spectrometry—0.5 μl of the sample solution in 0.1% trifluoroacetic acid was mixed on the sample plate with 0.5 μl of a saturated solution of 4-hydroxy-α-cyanocinnaminic acid in 50% acetonitrile, 0.1% trifluoroacetic acid containing insulin as the internal calibrant. The solution was air-dried before introduction into the mass spectrometer. Spectra were acquired on a PerSeptive Voyager-DE STR matrix-assisted laser desorption ionization time-of-flight instrument operated in reflectron delayed extraction mode (200 ns). The instrument was equipped with a nitrogen laser (3-ns pulse, 1950 power). The accelerating potential was 25 kV, and the grid voltage was 72%.

Sequencing—The toxin was further purified by microbore reversed-phase HPLC (0.8 × 250-mm C18 column, with a linear gradient from 15–70% B over 90 min, with a flow rate of 40 μl/min, monitored at 214 nm). The toxin peak was collected at 24.6 min. The HPLC fraction (~1 nmol) was dried down and taken up in 80 μl of 8 M guanidine-HCl, 100 mM Tris, 5 mM tributylphosphine at pH 8.5 and incubated for 8 h at 55 °C. *N*-Isopropyliodoactamide (1 mg in 20 μl of MeOH plus 80 μl of Tris) was added, and the solution was incubated for an additional 2 h at room temperature. The reduced and alkylated peptide was then desalted by HPLC on a C18 column as described above (elution time 30.1 min). N-terminal sequencing was carried out on an ABI 477 after loading the reduced and alkylated peptide on polyvinylidene difluoride membrane.

Digestion with BNPS-skatole was carried out by dissolving the purified reduced and alkylated peptide in 50 μl of 0.1% trifluoroacetic acid and 15 μl of BNPS-skatole. The solution was incubated at room temperature for 8 h. The digestion products were separated by HPLC as described above. Two main peaks were collected and sequenced by Edman degradation. Asp-N digestion was performed by dissolving the purified reduced and alkylated peptide in 100 mM Tris, pH 8.0, and treating with 1% (w/w) Asp-N for 20 h at 35 °C. The fragments were separated and analyzed by mass spectrometry prior to Edman degradation. For mass spectrometry, 1 μl of the sample solutions (intact toxin or fragments) in 0.1% trifluoroacetic acid (or the HPLC elution solvent) were mixed on the sample plate with 1 μl of a saturated solution of 4-hydroxy-α-cyanocinnamic acid in 50% acetonitrile, 0.1% trifluoroacetic acid. The solution was allowed to air-dry before being introduced into the mass spectrometer.

Astrocyte Cell Culture—Activated adult astrocytes isolated from gelatin-sponge implants taken from adult Sprague-Dawley rat brain were generously provided by Dr. Thomas Langan (SUNY Buffalo) at passage numbers 2–4. Astrocytes were maintained in Dulbecco's modified Eagle's medium, 10% fetal bovine serum, and 1% penicillin/streptomycin and were used in experiments between 2 and 5 days after passage. Cells between passages 4 and 35 expressed SACs with the same properties. Flat, polygonal, fibroblast-like cells and stellate cells were used.

Astrocyte Single Channel Patch Clamp—An Axopatch 200B (Axon Instruments) amplifier was used for patch clamping, whereas experimental protocols and data acquisition were controlled by Axon Instruments pClamp8 software via a Digidata 1322A acquisition system. Currents were sampled at 10 kHz and low pass-filtered at 2 kHz through the four-pole Bessel filter on the Axopatch 200B. All potentials are defined with respect to the extracellular surface. Electrodes were pulled on a model PC-84 pipette puller (Brown-Flaming Instruments, CA), painted with Sylgard 184 (Dow Corning Corp., Midland, MI) and fire-polished. Electrodes were filled with KCl saline (140 mM KCl, 5 mM EGTA, 2 mM $MgSO_4$, 10 mM Hepes, pH 7.3) and had resistances ranging from 6 to 8 megaohms. Bath saline consisted of 140 mM NaCl, 5 mM KCl, 2 mM $CaCl_2$, 0.5 mM $MgSO_4$, 6 mM glucose, and 10 mM Hepes, pH 7.3. Pressure and suction were applied to the pipette by a HSPC-1 pressure clamp (ALA Scientific Instruments) controlled by the pClamp software. Perfusion of toxin samples was performed by a pressurized local perfusion system BPS-8 (ALA Scientific Instruments) with eight separate channels. Off-line data analysis was performed with Clampfit and Origin 6.1 software.

Diffusional Translation—In order to determine whether the proteins were aggregated, the coefficients of self-diffusion (D_t) for GsMTx2 and GsMTx4 were measured using a longitudinal encode-decode pulse sequence (21) with the proteins lyophilized and resuspended in D_2O. Lysozyme was used as a standard control for slope calibration. D_t for 2 mM lysozyme in a $^1H_2O/^2H_2O$ mixture at 298 K was taken to be 1.08×10^{-6} cm^2 s^{-1} (21). Data from experiments utilizing 10 different gradient strengths, ranging from 4 to 60 gauss, were analyzed. Increments of ⅛, ¼, ½, and ¾ maximum were run in triplicate to provide estimates of error in the exponential fit. Peak intensities were fit to the equation,

$$\ln(I) = \ln(I_0) + G^2\gamma^2\delta^2(\Delta/3 - \delta/3)D_t \qquad \text{(Eq. 1)}$$

where I represents measured peak intensity, G is the gradient strength in gauss/cm, γ is the gyromagnetic ratio of protons (26,753 radian s^{-1} G^{-1}), δ is the length of the gradient pulse (1.5 ms), Δ is the diffusion time between gradients (600 ms), and D_t is the self-diffusion rate.

NMR Spectroscopy—Samples from the Vydac C18 column were lyophilized and resuspended in distilled H_2O to 2 mM toxin. The samples were then titrated to pH 4.5, and D_2O was added to 8%. A 250-μl aliquot of the protein solution was transferred to a 5-mm Shigemi tube for NMR spectroscopy. All experiments were performed on Varian Inova 600 and 500 spectrometers equipped with triple resonance Z-gradient probes at the Cornell Biomolecular NMR Center. Data were collected in States-TPPI mode (22) for quadrature detection. Homonuclear two-dimensional NOESY (23), TOCSY (24), and COSY (25) spectra were obtained at 5, 16, 20, 25, and 35 °C with presaturation during the recycle period followed by SCUBA recovery (26). A DIPSI-2 (27) sequence of 60–90 ms was used in the TOCSY experiments, and a 150-ms mixing period was used in the NOESY experiments. Two-dimensional $^1H,^{15}N$ HSQC and $^1H,^{13}C$ HSQC (28) spectra were acquired with natural abundance proteins. Data were processed either with a modification of version 2.3 of Felix software (Accelrys, Inc.) or NMRPipe (29). Sparky (30) was used for data visualization, assignments, and peak integration. Dihedral angle constraints were obtained from the chemical shift index (31–33) and from measurements of coupling constants using a two-dimensional COSY experiment with 8192 points in t2. Stereospecific assignments and χ_1 constraints were determined using an exclusive COSY (34) and the NOESY experiments.

Structure Calculation—Distance constraints for structural calculations were obtained from a series of two-dimensional homonuclear NOESY experiments at 5–35 °C in either 90% H_2O/10% D_2O or 100% D_2O. Distance constraints were classified into four categories according to the intensity of the NOE cross-peak (<2.4, <3.4, <4.0, and <5.5 Å). On the basis of the chemical shift index and coupling constants from a high resolution COSY experiment, backbone dihedral angles were constrained to favorable regions of ϕ,ψ space: α-helix, ϕ, −80 ± 30°; ψ, −20 ± 30°; β-strand, ϕ, −105 ± 65°; ψ, 145 ± 45° (35). χ_1 constraints and stereospecific assignments of β protons were made based on the exclusive COSY and NOESY spectra (36). The distance and dihedral

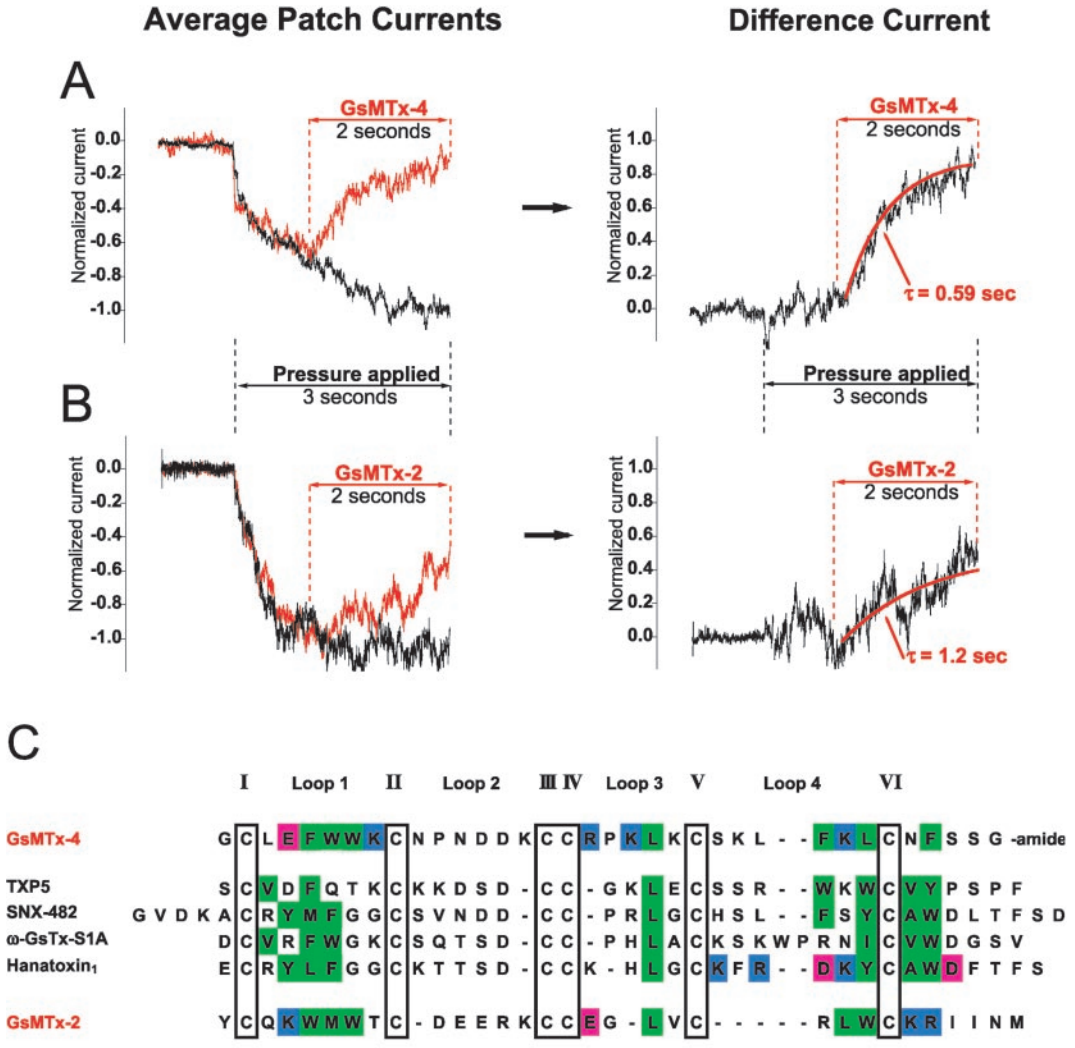

FIG. 1. **Comparison of GsMTx-4 and GsMTx-2 association rates and homology with other ICK motif peptides.** GsMTx-4 (*A*) and GsMTx-2 (*B*) inhibition of average MSC currents from rat astrocyte outside-out patches held at −50 mV. *A*, control current (*black*) is the average of 37 pressure steps ranging from 35 to 70 mm Hg, whereas the GsMTx-4 current (*red*) is the average of 29 pressure steps ranging from 38 to 80 mm Hg ($n = 7$ patches). *B*, control and GsMTx-2 currents; the average of 35 pressure steps ranging from 50 to 100 mm Hg ($n = 5$ patches). *Black bars*, pressure application; *red bars*, indicate peptide application. Difference currents are shown on the *right*. The difference currents were fit with a single exponential of the form $I = I_o + Ae^{-(\Delta t/\tau)}$ (*red curves*), and the time constants (τ) are shown *below* each *curve*. The steady state currents (I) used to calculate K_D were derived from the curve fit in the case of GsMTx-2, and the measured residual current from Fig. 6 in Ref. 14 for GsMTx-4. *C*, sequences of GsMTx-2 and GsMTx-4 with the four most homologous toxins to GsMTx-4 listed in order of their similarity. Sequences are aligned to show the ICK motif cysteine residues in *boxes*. *Green shaded* residues show conserved hydrophobic clusters that combine to form a hydrophobic patch on the folded peptides. *Blue* and *lavender* residues on GsMTx-4, GsMTx-2 and Hanatoxin show the positive and negative residues, respectively, that surround the hydrophobic face. Relative to GsMTx-4: TXP5, K^+ channel blocker (55), 40% identity and 54% similarity; SNX-482, blocks E-type Ca^{2+} channels (56), 40% identity and 49% similarity; ω-GramTX S1A, blocks N-, P-, and Q-type Ca^{2+} channels (not L-type) (57), 34% identity and 46% similarity; Hanatoxin, K^+ channel blocker (58), 28% identity and 37% similarity; GsMTx-2, 11% identity and 28% similarity.

restraints were used as inputs to determine preliminary structures using the distance geometry/simulated annealing protocol in CNS 1.0 (Crystallography and NMR System) (37). Hydrogen bonding constraints were added in subsequent calculations based on deuterium exchange data, characteristic NOE patterns (see Fig. 3), and likely hydrogen bonding partners determined from the preliminary structures. Three hundred structures were calculated using CNS, and the 20 lowest energy structures were aligned to the average structure using XPLOR version 3.851 (38). The structures were visualized using Swiss-PdbView (39) and analyzed using Procheck-NMR, Aqua (35), and NMR-CLUST (40). The hydrogen-bonding pattern was verified by recalculating a set of 200 structures without the hydrogen bonding constraints. The 20 lowest energy structures were analyzed. The NH and carbonyl oxygens of the hydrogen bonding pairs were oriented correctly in almost all structures, although in some cases, the distance between the NH and oxygen was somewhat greater than that observed when the hydrogen bonding constraints were included in the calculation.

RESULTS

Comparison of MSC Blocking Activity—G. spatulata whole venom was fractionated by reversed-phase HPLC, and fractions were superfused onto outside-out patches from rat astrocytes to assess MSC activity. Fractions that showed activity were again fractionated on successively shallower gradients until a single active component was isolated. Suchyna *et al.* (14) described the properties and primary structure of GsMTx-4, a peptide with the highest affinity of any known blocker of MSCs. At a concentration of 5 μM, GsMTx-4 blocked ~92% of the MSC current with an association rate of 3.4×10^5 M^{-1} s^{-1} (Fig. 1*A*). The ratio of association and dissociation rates produced an equilibrium constant of ~500 nM. A similar number resulted from treating the reaction as a simple bimolecular reaction and using the residual (steady state) current as a measure of the

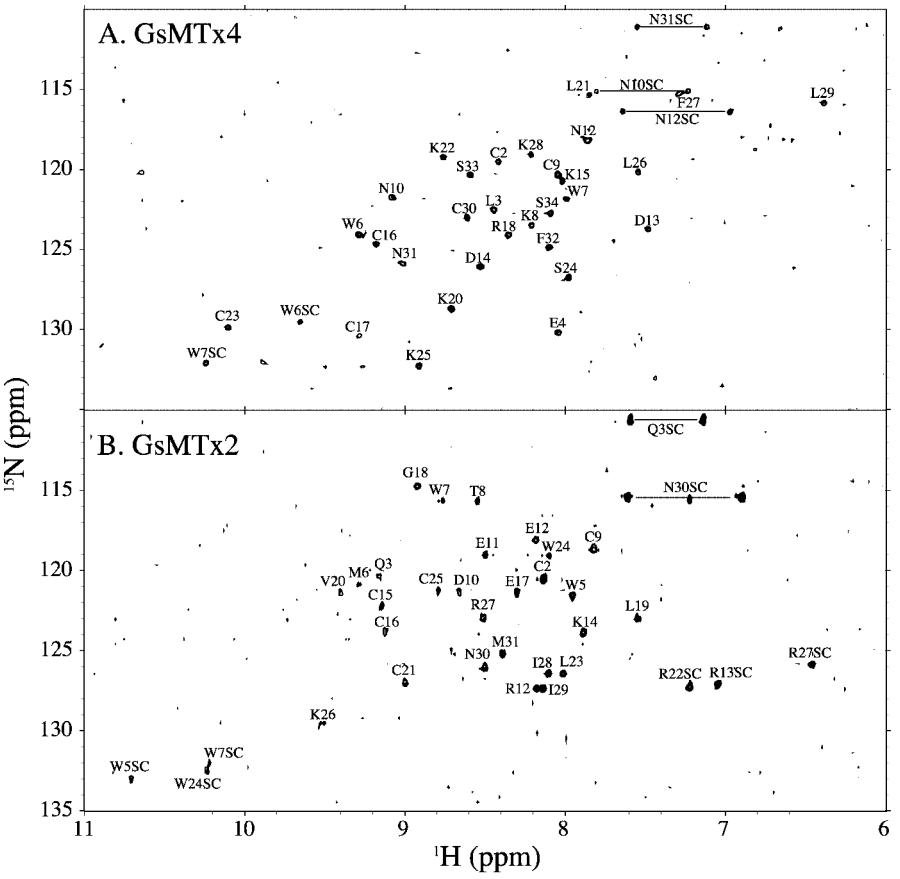

FIG. 2. **Natural abundance ^{1}H,^{15}N HSQC spectra of GsMTx-4 (*A*) and GsMTx-2 (*B*).** Data were collected at 600 MHz, averaging 512 transients at each of 128 complex increments. All backbone N-NH correlations were observed except for the N termini and Phe[5] of GsMTx-4. In addition, a number of side chain correlations were observed and are labeled. These are indicated with a suffix of *SC*.

unbound fraction (see Figs. 5 and 6 in Suchyna *et al.* (14)).

The largest HPLC peak in *Grammostola* whole venom was actually a complex of several peaks, one of which could block MSCs but showed lower activity than GsMtx-4. The active peak eluted at 21.5 min on a 15–50% acetonitrile 40-min linear gradient (see Fig. 3*A* in Ref. 14). At 5 μM, this peptide (designated GsMTx-2) blocks ~45% of the MSC current with an association rate constant of 1.7×10^5 M^{-1} s^{-1} (Fig. 1*B*). Assuming a single binding site, the ratio of the residual unblocked steady state current (I) to the peak current in the absence of toxin (I_o) is $I/I_o = 1/(1 + T/K_D)$, where T is the toxin concentration. For 5 μM GsMTx-2, I/I_o is 0.55, giving a K_D of ~6 μM. Thus, the affinity of GsMTx-2 for astrocyte MSCs is ~12 times lower than that of GsMTx-4.

Sequence Homology of Related Tarantula Toxins—The sequence of GsMTx-2 has less than 25% homology to GsMTx-4 as shown at the *bottom* of the sequence alignment in Fig. 1*C*. The four ICK tarantula peptides shown in the *middle* of Fig. 1*C* have the highest sequence similarity to GsMTx-4 (and higher than that of GsMTx-2) but are not mechanotoxins (toxins that inhibit MSCs). Given that the peptides that are not mechanotoxins have much higher sequence similarity to GsMTx-4 than GsMTx-2, the structures of GsMTx-2 and GsMTx-4 may provide clues as to the origin of specificity for MSCs.

Of the peptide sequences shown, three-dimensional structures only exist for Hanatoxin, GsMTx-2, and GsMTx-4 (see below). For these three peptides, the hydrophobic amino acids that form a cluster on the surface of the three peptides are shown in *green* (Fig. 1). Assuming structural homology, the corresponding hydrophobic amino acids on the other three toxins (TXP5, SNX-482, and ω-GsTx-S1A) are also shown in *green*. The hydrophobic patch of Hanatoxin has been suggested to be part of the channel-binding domain, based on homology to other toxins. The charged residues that surround the hydrophobic patch are shown in *blue* (+) and *lavender* (−), but since their sequence positions vary significantly, the charges are only marked on the toxins where structures are known.

Diffusion Measurements—In order to determine whether GsMTx2 and GsMTx4 were aggregated in the samples used for NMR spectroscopy, D_t was measured at 500 MHz using a pulsed field gradient method (21) with lysozyme as a standard. Plots of ln(I) *versus* G^2 (Equation 1) were linear over the range of gradient strengths used for experiments for all three proteins (the two toxins and lysozyme). The average D_t for GsMTx2 was 2.26×10^{-6} cm^2 s^{-1}, and that for GsMTx4 was 2.22×10^{-6} cm^2 s^{-1}. Using the known hydrodynamic radius of lysozyme (R_h = 20.5 Å), R_h of GsMTx2 and GsMTx4 could be estimated as ~12.8 and 13.3 Å, respectively (41). These values are what would be expected given the empirical relationship, $R_h = 4.75n^{0.29}$, for the hydrodynamic radius of a globular protein having n = 31 and 35 amino acids (41). Likewise, these values are consistent with the overall shape and dimensions of the calculated structures described below, confirming that, under the conditions used, both toxins are monomeric.

Resonance Assignments and Torsion Angles—Sequence-specific resonance assignments (excluding the first residue) were made for both peptides using both homonuclear and heteronuclear experiments. A natural abundance ^{1}H,^{15}N HSQC experiment provided a fingerprint of the amide nitrogen and amide proton correlation for each residue except proline (Fig. 2). Homonuclear TOCSY, DQF-COSY, and NOESY experiments were then used to do the bulk of the assignments, which employed standard techniques (42). The assignments were assisted by the analysis of a ^{1}H,^{13}C HSQC spectrum. Using the proton chemical shifts in this spectrum, the peaks could be assigned to a particular spin system by comparison with the TOCSY experiment. The corresponding carbon chemical shift of the C$^{\alpha}$ and C$^{\beta}$ could then be used to aid in identification of

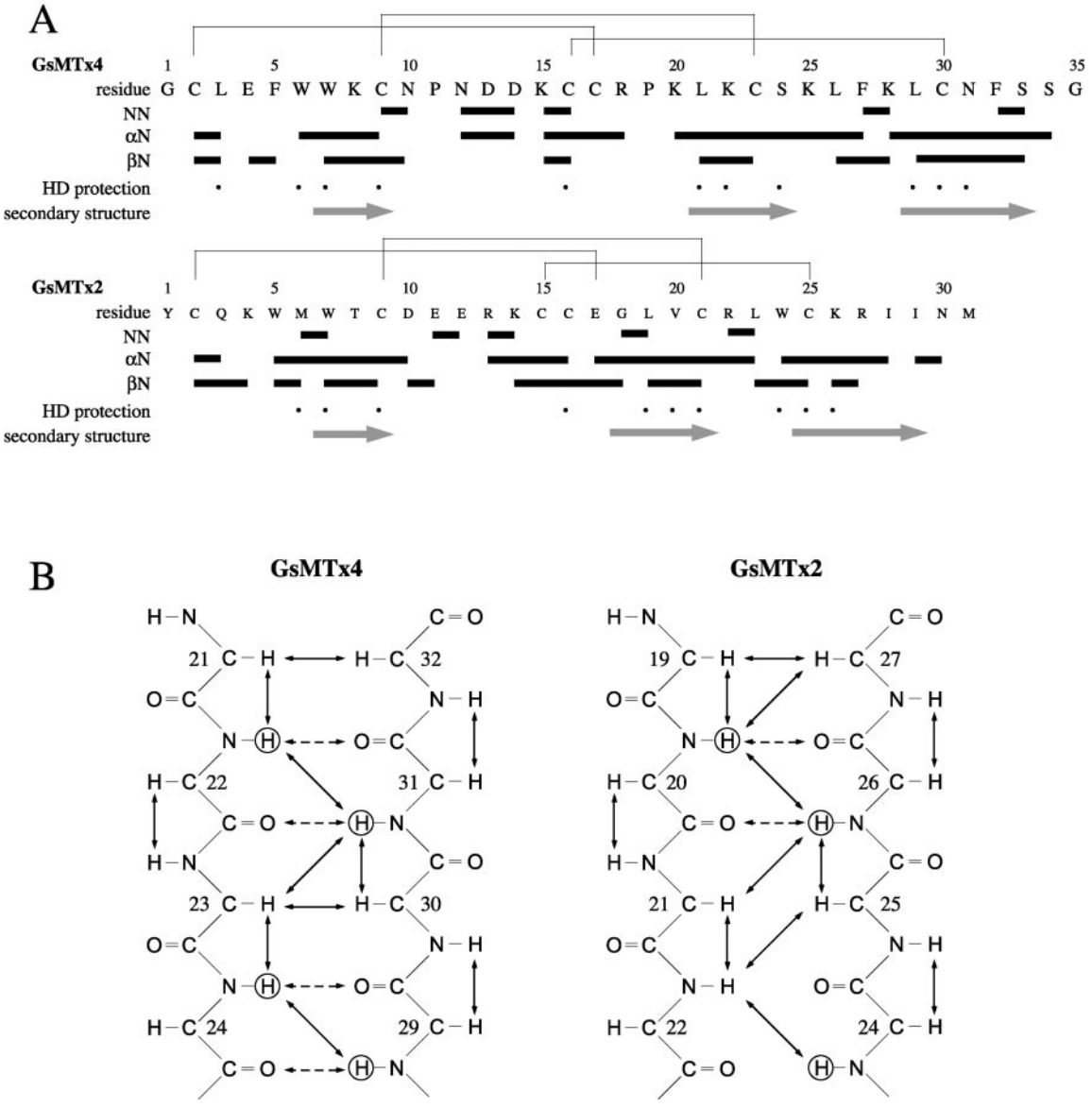

FIG. 3. **Summary of the assignments and secondary structure of GsMTx-4 and GsMTx-2.** *A*, NOEs between backbone atoms used to make sequential assignments are indicated with a *line*. Residues for which the amide proton-deuterium exchange was slower than 1 day are shown with a *dot*. The *arrows* indicate the position of the β strands. *B*, schematic of the antiparallel β sheet in both GsMTx-4 and GsMTx-2. Amide protons exhibiting slow exchange with solvent are *circled*. Observed NOEs are shown with *arrows*, and hydrogen bonds used in the structural calculations (inferred from the NOEs and hydrogen-deuterium exchange) are shown with *dashed arrows*.

the amino acid type. Backbone NOEs used to make sequential assignments and to aid in the assignment of hydrogen bonds are summarized in Fig. 3*A*. Using chemical shift index analysis and analysis of the high resolution DQF-COSY spectra, a total of 14 (GsMTx-4) and 17 (GsMTx-2) ϕ,ψ distance constraints were obtained.

Disulfide-bonding Pattern—Characteristic of the ICK motif, both GsMTx-2 and GsMTx-4 exhibit three disulfide bonds in relatively close proximity. For GsMTx-4, if the structures are calculated without assuming a disulfide-bonding pattern, the bond between Cys^2 and Cys^{17} can clearly be assigned due to the proximity of the two side chains and an NOE between an H^β of Cys^2 and an H^β of Cys^{17}. Of the remaining four cysteines, Cys^9 is positioned close to both Cys^{30} and Cys^{23} (3.69 ± 0.32 Å and 4.13 ± 0.69 Å, respectively). If one assumes a disulfide bond between Cys^9 and Cys^{30}, then Cys^{16} and Cys^{23} would not be positioned correctly to form a disulfide (9.51 ± 0.99 Å apart). On the other hand, if Cys^9 formed a disulfide with Cys^{23}, then Cys^{30} could easily form a disulfide with Cys^{16}. This pattern is supported by an observed NOE between an H^β of Cys^{16} and an H^β of Cys^{30}. The lowest energy structures and lowest r.m.s. deviations were obtained from structures with explicit disulfides between Cys^9–Cys^{23} and Cys^{16}–Cys^{30} as opposed to the two other possible patterns (Cys^9–Cys^{30}/Cys^{16}–Cys^{23} and Cys^9–Cys^{16}/Cys^{23}–Cys^{30}). In order to test this pattern further, structures were calculated, restraining the disulfide dihedral to within ±10° of the ideal values (*i.e.* 90 ± 10° and −90 ± 10°). 50 structures were calculated for each of three combinations of disulfide bonds holding 2–17 constant (Cys^9–Cys^{23}/Cys^{16}–Cys^{30}, Cys^9–Cys^{30}/Cys^{16}–Cys^{23}, and Cys^9–Cys^{16}/Cys^{23}–Cys^{30}) and each of eight combinations of two dihedral constraints (90 ± 10° and −90 ± 10°) on the three disulfides (*i.e.* 400 structures for each of the three disulfide-bonding patterns). For Cys^2–Cys^{17}/Cys^9–Cys^{30}/Cys^{16}–Cys^{23}, less than 3% of the structures had no NOE violations, and all had relatively high overall energies. Both Cys^2–Cys^{17}/Cys^9–Cys^{23}/Cys^{16}-Cys^{30} and Cys^2–Cys^{17}/Cys^9–Cys^{16}/Cys^{23}–Cys^{30} produced structures with no NOE violations (56 and 45% of the 400 structures, respective-

ly), but the energies were 50% higher for the Cys^2–Cys^{17}/Cys^9–Cys^{16}/Cys^{23}–Cys^{30} structures. Thus, given the specific NOEs between H^β atoms, the distances between S^γ atoms in the structures calculated without disulfide distance constraints, and the overall energy terms with and without disulfide dihedral constraints, the Cys^2–Cys^{17}/Cys^9–Cys^{23}/Cys^{16}–Cys^{30} pattern was used for all subsequent refinement. Given this dihedral bonding pattern, the dihedral angle for Cys^{16}–Cys^{30} could be uniquely defined as approximately −90°, since the lowest overall energies were produced with this constraint. The dihedral angles for Cys^2–Cys^{17} and Cys^9–Cys^{23} were not as well defined. Considering the structures calculated without disulfide dihedral constraints, the dihedral angles for Cys^2–Cys^{17} and Cys^9–Cys^{23} cluster in the range of 80–120° for the majority of the structures (80% for both Cys^2–Cys^{17} and Cys^9–Cys^{23}), whereas the remainder are either extended (−135° to −170°) for Cys^2–Cys^{17} or in the range of −95° to −105° for Cys^9–Cys^{23}. In the case of Cys^{16}–Cys^{30}, the disulfide dihedrals cluster in the range of −70° to −110° for the majority of structures (65%), whereas the remainder are extended, with none near 90°. Given the propensity of Cys^2–Cys^{17} and Cys^9–Cys^{23} to cluster near 90° and Cys^{16}–Cys^{30} to cluster near −90°, a final series of 200 structures were calculated with and without these disulfides constrained to within ±10° of the ideal values (*i.e.* 90 ± 10° for Cys^2–Cys^{17} and Cys^9–Cys^{23} and −90 ± 10° for Cys^{16}–Cys^{30}). No significant differences in overall energy or r.m.s. deviation were observed with these constraints or without these constraints. In summary, the disulfide-bonding pattern consisting of Cys^2–Cys^{17}/Cys^9–Cys^{23}/Cys^{16}–Cys^{30} was most consistent with the data, with a disulfide dihedral for Cys^{16}–Cys^{30} of approximately −90° and the dihedrals for Cys^9–Cys^{23} and Cys^{16}–Cys^{30} of approximately +90°.

A similar strategy was used to define the disulfide-bonding pattern of GsMTx2, the pattern was even more apparent from the differences in the quality of the structures. Both the Cys^2–Cys^{16} (homologous to Cys^2–Cys^{17} of GsMTx4) bond and the Cys^{15}–Cys^{25} (homologous to Cys^{16}–Cys^{30} of GsMTx4) were apparent from the structure calculated without assuming a disulfide-bonding pattern. Explicitly defining the Cys^2–Cys^{17}, Cys^{15}–Cys^{25}, Cys^9–Cys^{21} pattern provided the lowest energy structures of all those tested. Finally, restraining the disulfides to within ±10° of the ideal values produced lower energy structures for the Cys^2–Cys^{17}, Cys^{15}–Cys^{25}, Cys^9–Cys^{21} pattern, as described above for GsMTx4, although within this disulfide-bonding pattern, several combinations of dihedral angles produced low energy structures. Thus, the disulfide-bonding pattern is conserved between GsMTx2 and GsMTx4 and is similar to other ICK proteins (16).

Structural Analysis—Overlays of the 20 lowest energy structures of GsMTx-2 and GsMTx-4 are shown in Fig. 4*A*, and the structural statistics are given in Table I. As discussed above, the structures of both GsMTx-2 and GsMTx-4 have three disulfide bonds (I–IV, II–V, III–VI; see Figs. 1*C* and 3*A*) typical of the ICK motif (16, 17) and exhibit a secondary structure (Figs. 3*B* and 4*B*) characteristic of other ICK proteins (*e.g.* ω-conotoxin GVIA (43), a calcium channel blocker). The secondary structure is composed of three β strands, two of which form an antiparallel β sheet (Fig. 3*B*) and a third that crosses over the first two (Fig. 4*B*). As is typical of the ICK motif, the disulfide III–VI penetrates a ring formed by the other two disulfide bonds. The N and C termini in both structures show some disorder, which is a reflection of the lack of long range NOEs to constrain this region of the protein. Likewise, in both proteins, loops 2 and 4 are somewhat less well defined relative to the remainder of the protein (Fig. 4*A*). Backbone dynamics studies of a structurally related protein (precursor form of ω-conotoxin MVIIA) (44) are consistent with chemical exchange processes in the corresponding portions of the peptide. This would suggest that at least two loops of the protein not directly involved in secondary structure show mobility on the millisecond time scale.

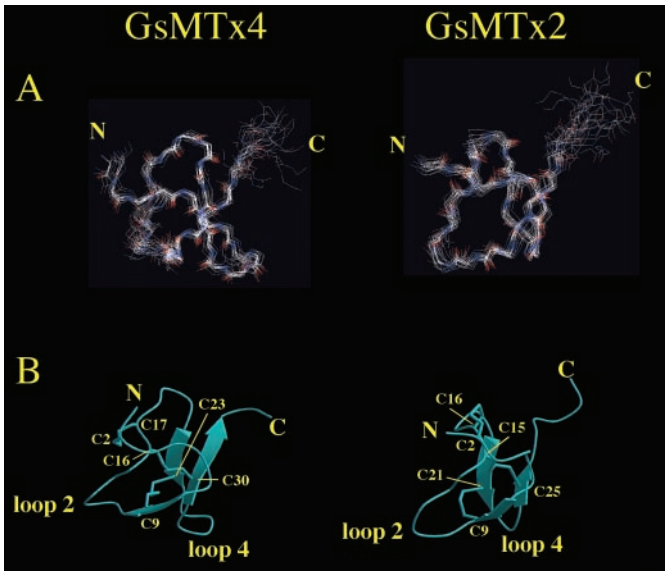

FIG. 4. **Three-dimensional structures of GsMTx-4 and GsMTx-2.** *A*, overlay of the 20 lowest energy structures for both peptides. The structures were superimposed using the backbone atoms between the first and sixth cysteine. Deviations of the structure from the average structure are given in Table I. The *figure* was prepared using Swiss-PdbView (39). *B*, The most representative structure (40) from each of the peptides is shown with the secondary structure indicated. The *figure* was rendered using Molscript (59) and Raster3D (60).

DISCUSSION

Homology among Structures Suggests Function—Although none of the tarantula toxins shown in Fig. 1*C* have more than 50% sequence homology to GsMTx-4, two common features are immediately apparent from the primary sequences: 1) the intercysteine spacing requiring only a few space substitutions for proper alignment and 2) the hydrophobic amino acids that form two clusters at the ends of the peptides around a conserved central leucine located two residues upstream of cysteine V (Fig. 1*C*). Because the structure of Hanatoxin has been solved (19) and its inhibitory function has been thoroughly studied (45–48), it can guide predictions about the structure and function of GsMTx-2 and GsMTx-4. However, it should be noted that no mutagenesis studies have been reported on any of the toxins listed in Fig. 1*C* to delineate their sensitive residues. Hanatoxin and GsTx-S1A have both been shown to be gating modifiers of their respective targets (49), but the inhibitory mechanisms of GsMTx-2 and GsMTx-4 have not yet been determined.

The distribution of charges on Hanatoxin shows a hydrophobic patch surrounded by charged residues that have been suggested to interact directly with K^+ channels. Identification of this region as the binding interface is based on the structures of other toxins that have been shown to modify gating and on receptor mutagenesis studies (50). A similar hydrophobic patch in GsMTx-2 and GsMTx-4 (Fig. 5*A*) is formed by the aromatic residues in loop 1 and those surrounding cysteine VI (Fig. 1*C*). All hydrophobic/aromatic residues in these three peptides contribute to the hydrophobic patch. The patch may be involved in the binding interface, but is unlikely to provide specificity for binding to MSCs, since most of the hydrophobic amino acids are spatially conserved among GsMTx-4, GsMTx-2, and Hanatoxin (Fig. 5*B*, 0° orientation). The backbone folds of the three pep-

TABLE I
Structural statistics

	GsMTx-4	GsMTx-2
Coordinate precision[a]		
r.m.s. deviation CO, C^{α}, N residues (Å)[b]	0.61 ± 0.20	0.56 ± 0.15
r.m.s. deviation heavy atom residues (Å)	1.17 ± 0.21	1.25 ± 0.21
Statistics for structure calculation		
r.m.s. deviation from experimental restraints		
NOE distances (Å)	0.024 ± 0.001	0.020 ± 0.003
Dihedral angles (degrees)	0.34 ± 0.05	0.24 ± 0.08
r.m.s. deviation over secondary structure		
Bonds (Å)	0.002 ± 0.0001	0.002 ± 0.0002
Angles (degrees)	0.38 ± 0.02	0.43 ± 0.02
Impropers (degrees)	0.18 ± 0.02	0.26 ± 0.04
Procheck analysis		
Most favored (%)	49.7	49.5
Additional allowed (%)	45.2	35.0
Generously allowed (%)	1.6	6.2
Disallowed region (%)	3.5	9.3

[a] Determined from the 20 lowest energy structures relative to the average of the 20 structures calculated by XPLOR (38).
[b] r.m.s. deviations were calculated over residues 2–31 on GsMTx-4 and residues 2–25 on GsMTx-2.

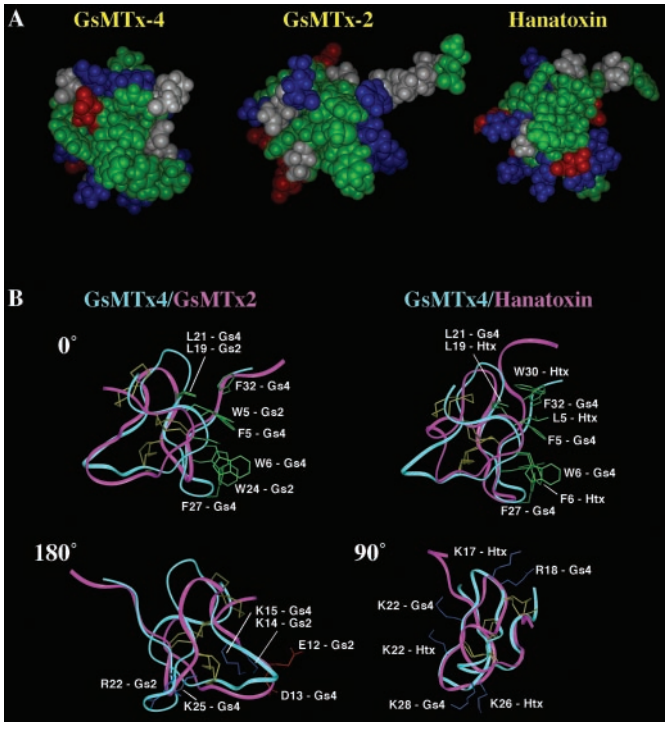

FIG. 5. **Comparison of the GsMTx-4 structure with GsMTx-2 and with Hanatoxin, a homologous toxin ineffective on MSCs.** *A*, space-filling models of GsMTx-4, GsMTx-2, and Hanatoxin are shown. Aromatic and hydrophobic residues are shown in *green*, positively charged residues are shown in *blue*, and negatively charged residues are shown in *red*. *B*, the backbones of Hanatoxin and GsMTx-2 (*magenta ribbons*) are aligned with the backbone of GsMTx-4 (*cyan ribbons*). The three disulfide bonds are shown in *yellow*. 0° orientation (same as the orientation in *A*) has labeled aromatic groups (*green*) that share spatially equivalent domains. All appear along one face of the peptides. The 180° and 90° orientations have spatially equivalent charged residues labeled (*red*, negative; *blue*, positive). The position of the equivalent charged residues in the two mechanotoxins differs significantly from the homologous groups shared by GsMTx-4 and Hanatoxin.

tides and the disulfide bonds are nearly superimposable, allowing us to reliably predict the spatially conserved residues. The centrally located, conserved leucine is particularly striking, since it shares a nearly identical spatial position among all three peptides. It is positioned internally, beneath the hydrophobic patch (Fig. 5*B*, 0° orientation), allowing it to interact with the hydrophobic side chains on the surface. It may act to stabilize the patch and/or facilitate folding and disulfide formation. Adding to speculation that the hydrophobic patch may be involved in binding, Phe^{5} in GsMTx-4 was the only amino acid besides the terminal glycines and prolines that could not be assigned in the $^{1}H,^{15}N$ HSQC spectrum of GsMTx-4 (Fig. 2). A weak signal may indicate significant chemical exchange on the NMR time scale, suggesting a relatively high flexibility. Flexible regions of proteins (loop regions in particular) may be important for facilitating the induced fit that occurs during protein-protein interactions (51–54). In this regard, loops 2 and 4 are also less well defined than the rest of the protein (excluding the flexible N and C termini).

It has been suggested that the charged residues surrounding the hydrophobic patch of Hanatoxin may be important for toxin binding. The locations of charged residues that surround the hydrophobic patch vary significantly as illustrated by *highlighted residues* in Fig. 1*C* for the structurally determined toxins. One notable feature of GsMTx-4 is that whereas all six peptides shown in Fig. 1*C* have a similar total number of charged residues (from 8 to 11), GsMTx-4 has a net positive charge of +5 compared with +2 or −2 for the other five peptides. However, charge itself is not the key variable, since we found that di- and trilysines have no effect on the open probability (data not shown). Thus, the distribution of charges displayed on the ICK scaffold may be the critical determinant in receptor selectivity.

Significant differences arise in the distribution of charged residues surrounding the hydrophobic patch (Fig. 1*C*, *blue* and *lavender highlighted residues*). The overall distribution of charged residues around the hydrophobic patch can be viewed in the orientation shown in Fig. 5*A*. Establishing the contribution of each side chain to specificity will require mutagenesis studies. Although there is little overlap of charged residues on the surfaces shown in Fig. 5*A*, GsMTx-4 and GsMTx-2 do share a unique feature away from the hydrophobic patch. Both mechanotoxins have a series of negatively charged residues followed by one or two positively charged residues immediately preceding cysteine III (GsMTx-4, Asp^{13}–Lys^{15}; GsMTx-2, Asp^{10}–Lys^{14}; Fig. 1*C*). The other nonmechanotoxins have only negative charges preceding cysteine III. Furthermore, two of these charged residues (GsMTx-4, Asp^{13} and Lys^{15}; GsMTx-2, Glu^{12} and Lys^{14}) share similar spatial positions (Fig. 5*B*, 180° orientation). This charged sequence lies in loop 2, one of the more flexible regions of the protein described above. On loop 4, the other flexible region of the peptide, positively charged residues with similar spatial positions extend from all three peptides

but in different positions for the mechanotoxins (Lys^{25}/Arg^{22} for GsMTx-4/GsMTx-2 and Lys^{28}/Lys^{26} for GsMTx-4/Hanatoxin, respectively).

Although other *Grammostola* toxins (Hanatoxin and ω-GsTx-S1A) are more homologous to GsMTx-4 than GsMTx-2, they were not identified as MSC blockers during screening of fractions from whole venom. If we assume the same inhibitory mechanism for both GsMTx-2 and GsMTx-4, the few similarities that exist between them could be useful for predicting residues involved in binding. Because cation-selective MSCs have not been cloned, these toxins may be useful tools in determining physiological function and histological distribution as well as assisting in receptor isolation. Whereas the relatively low affinity of both mechanotoxins makes histological studies and receptor isolation difficult, the three-dimensional structure will guide the interpretation of mutagenesis studies aimed at increasing peptide specificity.

Acknowledgments—We thank Dr. Michael Sutcliffe (University of Leicester) for helpful discussions. We thank the Laboratory of Chemical Physics at the National Institutes of Health and Frank Delaglio for making available the program NMRPipe, which was useful in analyzing NMR data.

Note Added in Proof—We recently determined the cDNA sequence for GsMTx-4 and it differed from the published sequence that was determined directly from the protein. The new C-terminal sequence is Ser-Phe-amide. It should replace the published C-terminal sequence Ser-Ser-Gly-amide. The molecular mass of the peptide with the corrected sequence matches the experimentally determined exact mass (4092.96 Da, MH^+ ion) of the wild-type toxin. In retrospect, a weak Phe peak is visible in the original peptide sequencing chromatograms. No differences were observed in the recalculated structure since this region of the protein is part of the unstructured C terminus.

REFERENCES

1. Sachs, F., and Morris, C. E. (1998) in *Reviews of Physiology, Biochemistry, and Pharmacology* (Blaustein, M. P., Greger, R., Grunicke, H., Jahn, R., Mendell, L. M., Miyajima, A., Pette, D., Schultz, G., and Schweiger, M., eds) pp. 1–78, Springer, Berlin
2. Chang, G., Spencer, R. H., Lee, A. T., Barclay, M. T., and Rees, D. C. (1998) *Science* **282,** 2220–2226
3. Patel, A. J., Honore, E., Maingret, F., Lesage, F., Fink, M., Duprat, F., and Lazdunski, M. (1998) *EMBO J.* **17,** 4283–4290
4. Patel, A. J., and Honore, E. (2001) *Trends Neurosci.* **24,** 339–346
5. Patel, A. J., Lazdunski, M., and Honore, E. (2001) *Curr. Opin. Cell Biol.* **13,** 422–428
6. Hamill, O. P., and Martinac, B. (2001) *Physiol. Rev.* **81,** 685–740
7. Ermakov, Y. A., Averbakh, A. Z., Yusipovich, A. I., and Sukharev, S. (2001) *Biophys. J.* **80,** 1851–1862
8. Ermakov Yu, A., Averbakh, A. Z., Arbuzova, A. B., and Sukharev, S. I. (1998) *Membr. Cell Biol.* **12,** 411–426
9. Ermakov Yu, A., Averbakh, A. Z., and Sukharev, S. I. (1997) *Membr. Cell Biol.* **11,** 539–554
10. Hackney, C. M., and Furness, D. N. (1995) *Am. J. Physiol.* **268,** C1–C13
11. Hamill, O. P., and McBride, D. W., Jr. (1996) *Pharmacol. Rev.* **48,** 231–252
12. Rusch, A., Kros, C. J., and Richardson, G. P. (1994) *J. Physiol.* **474,** 75–86
13. Small, D. L., and Morris, C. E. (1995) *Br. J. Pharmacol.* **114,** 180–186
14. Suchyna, T. M., Johnson, J. H., Hamer, K., Leykam, J. F., Gage, D. A., Clemo, H. F., Baumgarten, C. M., and Sachs, F. (2000) *J. Gen. Physiol.* **115,** 583–598
15. Bode, F., Sachs, F., and Franz, M. R. (2001) *Nature* **409,** 35–36
16. Craik, D. J., Daly, N. L., and Waine, C. (2001) *Toxicon* **39,** 43–60
17. Norton, R. S., and Pallaghy, P. K. (1998) *Toxicon* **36,** 1573–1583
18. McNulty, J. C., Thompson, D. A., Bolin, K. A., Wilken, J., Barsh, G. S., and Millhauser, G. L. (2001) *Biochemistry* **40,** 15520–15527
19. Takahashi, H., Kim, J. I., Min, H. J., Sato, K., Swartz, K. J., and Shimada, I. (2000) *J. Mol. Biol.* **297,** 771–780
20. Bascur, L., Yevenes, I., and Adrian, H. (1980) *Toxicon* **18,** 224
21. Altieri, A. S., Hinton, D. P., and Byrd, R. A. (1995) *J. Am. Chem. Soc.* **117,** 7566–7567
22. States, D. J., Haberkorn, R. A., and Ruben, D. J. (1982) *J. Magn. Reson.* **48,** 286–292
23. Kumar, A., Ernst, R. R., and Wüthrich, K. (1980) *Biochem. Biophys. Res. Commun.* **95,** 1–6
24. Braunschweiler, L., and Ernst, R. R. (1983) *J. Mag. Res.* **53,** 521–528
25. Aue, W. P., Bartholdi, E., and Ernst, R. R. (1976) *J. Chem. Phys.* **64,** 2229–2246
26. Brown, S. C., Weber, P. L., and Mueller, L. (1988) *J. Mag. Res.* **77,** 166–169
27. Rucker, S. P., and Shaka, A. J. (1989) *Mol. Phys.* **68,** 509–517
28. Bodenhausen, G., and Ruben, D. J. (1980) *Chem. Phys. Lett.* **69,** 185–189
29. Delaglio, F., Grzesiek, S., Vuister, G., Zhu, G., Pfeifer, J., and Bax, A. (1995) *J. Biomol. NMR* **6,** 277–293
30. Goddard, T. D., and Kneller, D. G., *Sparky*, Version 3, University of California, San Francisco
31. Wishart, D. S., Sykes, B. D., and Richards, R. M. (1991) *J. Mol. Biol.* **222,** 311–333
32. Wishart, D. S., Sykes, B. D., and Richards, F. M. (1992) *Biochemistry* **31,** 1647–1651
33. Wishart, D. S., and Sykes, B. D. (1994) *J. Biomol. NMR* **4,** 171–180
34. Griesinger, C., Sorensen, O. W., and Ernst, R. R. (1987) *J. Magn. Res.* **75,** 747–792
35. Laskowski, R. A., Rullmannn, J. A., MacArthur, M. W., Kaptein, R., and Thornton, J. M. (1996) *J. Biomol. NMR* **8,** 477–486
36. Wagner, G., Braun, W., Havel, T. F., Schaumann, T., Go, N., and Wüthrich, K. (1987) *J. Mol. Biol.* **196,** 611–639
37. Brunger, A. T., Adams, P. D., Clore, G. M., DeLano, W. L., Gros, P., Grosse-Kunstleve, R. W., Jiang, J. S., Kuszewski, J., Nilges, M., Pannu, N. S., Read, R. J., Rice, L. M., Simonson, T., and Warren, G. L. (1998) *Acta Crystallogr. Sect. D Biol. Crystallogr.* **54**, 905–921
38. Brunger, A. T. (1996) *Xplor Manual: Version 3.843*, Yale University
39. Guex, N., and Peitsch, M. C. (1997) *Electrophoresis* **18,** 2714–2723
40. Kelley, L. A., Gardner, S. P., and Sutcliffe, M. J. (1996) *Protein Eng.* **9,** 1063–1065
41. Wilkins, D. K., Grimshaw, S. B., Receveur, V., Dobson, C. M., Jones, J. A., and Smith, L. J. (1999) *Biochemistry* **38,** 16424–16431
42. Wüthrich, K. (1986) *NMR of Proteins and Nucleic Acids*, John Wiley & Sons, Inc., New York
43. Pallaghy, P. K., and Norton, R. S. (1999) *J. Pept. Res.* **53,** 343–351
44. Goldenberg, D. P., Koehn, R. E., Gilbert, D. E., and Wagner, G. (2001) *Protein Sci.* **10,** 538–550
45. Li-Smerin, Y., and Swartz, K. J. (2000) *J. Gen. Physiol.* **115,** 673–684
46. Li-Smerin, Y., and Swartz, K. J. (2001) *J. Gen. Physiol.* **117,** 205–218
47. Swartz, K. J., and MacKinnon, R. (1997) *Neuron* **18,** 675–682
48. Winterfield, J. R., and Swartz, K. J. (2000) *J. Gen. Physiol.* **116,** 637–644
49. Li-Smerin, Y., and Swartz, K. J. (1998) *Proc. Natl. Acad. Sci. U. S. A.* **95,** 8585–8589
50. Takahashi, H., Nakanishi, T., Kami, K., Arata, Y., and Shimada, I. (2000) *Nat. Struct. Biol.* **7,** 220–223
51. Demchenko, A. P. (2001) *J. Mol. Recognit.* **14,** 42–61
52. Gizachew, D., and Oswald, R. E. (2001) *Biochemistry* **40,** 14368–14375
53. Loh, A. P., Guo, W., Nicholson, L. K., and Oswald, R. E. (1999) *Biochemistry* **38,** 12547–12557
54. Luque, I., and Freire, E. (2000) *Proteins* **41,** Suppl. 4, 63–71
55. Kaiser, I. I., Griffin, P. R., Aird, S. D., Hudiburg, S., Shabanowitz, J., Francis, B., John, T. R., Hunt, D. F., and Odell, G. V. (1994) *Toxicon* **32,** 1083–1093
56. Newcomb, R., Szoke, B., Palma, A., Wang, G., Chen, X., Hopkins, W., Cong, R., Miller, J., Urge, L., Tarczy-Hornoch, K., Loo, J. A., Dooley, D. J., Nadasdi, L., Tsien, R. W., Lemos, J., and Miljanich, G. (1998) *Biochemistry* **37,** 15353–15362
57. Lampe, R. A., Defeo, P. A., Davison, M. D., Young, J., Herman, J. L., Spreen, R. C., Horn, M. B., Mangano, T. J., and Keith, R. A. (1993) *Mol. Pharmacol.* **44,** 451–460
58. Swartz, K. J., and MacKinnon, R. (1995) *Neuron* **15,** 941–949
59. Kraulis, P. J. (1991) *J. Appl. Crystallogr.* **24,** 946–950
60. Merritt, E. A., and Murphy, M. E. P. (1994) *Acta Crystallogr. Sect. D Biol. Crystallogr.* **50,** 869–873